Microwave Characterization of a Microstrip Line Using a Two-Port Ring Resonator With an Improved Lumped-Element Model

Joey R. Bray, *Student Member, IEEE,* and Langis Roy, *Member, IEEE*

***Abstract*—A two-port ring resonator is used to characterize the microwave properties of a microstrip line printed on Ferro A6-S low-temperature co-fired ceramic. The ring and its coupling gaps are simulated using a simple lumped-element model. The coupling gaps are modeled as capacitors, the values of which are extracted using a commercial two-and-one-half-dimensional electromagnetic simulator. The validity of the lumped-element model is assessed by comparing the simulated and experimental resonant frequencies and, for the first time, the simulated magnitudes of both the reflection and transmission coefficients are also compared with those obtained experimentally. A correction for the frequency pushing due to the capacitive loading of the coupling gaps is also presented. The resulting model is then shown to predict the resonant frequencies to within 0.11% from 5 to 40 GHz. The simulated and experimental reflection magnitudes are within 0.5 dB across the band, whereas the transmission magnitudes are within 3.5 dB up to 22 GHz. Experimental results indicate that the loss of the microstrip ranges from approximately 0.11 to 0.42 dB/cm across the band and that the relative permittivity of the substrate is nearly constant versus frequency with an average value of 6.17.**

***Index Terms*—Attenuation and permittivity measurements, equivalent lumped elements, resonant frequency, ring resonator.**

I. Introduction

RESONATORS have long been used to characterize the microwave properties of materials [1]. For planar circuitry, resonator configurations such as rings, half-wavelength lines, and others have been used to characterize both the attenuation of the medium and the substrate permittivity, which are obtained via a single swept frequency measurement [2]–[4]. The simple geometry of these resonators, combined with the relative ease of their analysis, contribute to their popularity, especially for benchmarking purposes. When a resonator is included during the fabrication of a larger panel, its electrical properties may be considered as representative of the other circuits contained on that panel, thereby making the resonator a convenient means for providing quality assurance.

In this paper, the one-port gap-coupled microstrip ring model introduced by Yu is expanded to the case of a two-port ring [5]. This lumped-element model is an attractive one because it does not require complex simulation tools, as discussed in Section II. The resonator theory leading to the characterization of the microstrip line is presented in Section III, whereas Section IV presents the manufactured ring and the evaluation of its attenuation constant. Capacitors are used in the lumped-element model to represent the coupling gaps. In Section V, a method is presented by which these capacitor values are extracted using a commercial two-and-one-half-dimensional (2.5-D) electromagnetic (EM) solver. The frequency pushing effect of the coupling gaps is analyzed in Section VI and a correction is then applied to the observed resonant frequencies of the ring, from which the dielectric constant of the substrate is finally obtained. The paper concludes with a simulation of the two-port ring resonator using the material parameters that were experimentally obtained, which demonstrates the accuracy of the model.

Manuscript received July 23, 2002; revised January 9, 2003. This work was supported in part by EMS Technologies under an Ontario Graduate Scholarship in Science and Technology.

The authors are with the Department of Electronics, Carleton University, Ottawa, ON, Canada K1S 5B6 (e-mail: jbray@doe.carleton.ca; lroy@doe.carleton.ca).

Digital Object Identifier 10.1109/TMTT.2003.810136

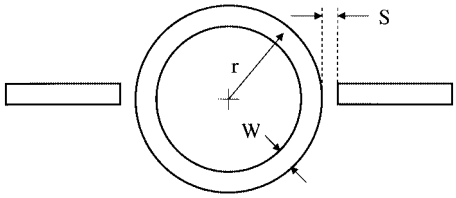

Fig. 1. Layout of a two-port co-linear-fed microstrip ring resonator.

II. Two-Port Ring Resonator Theory

A top view of the two-port co-linear-fed microstrip ring under consideration in this paper is shown in Fig. 1, where r is the mean radius, W is the microstrip linewidth, and S is the length of the coupling gap. Before considering the entire circuit, the input impedance of the ring alone is obtained. The model of the unloaded ring resonator is shown in Fig. 2(a) [5]. Here, the ring is conceptually split into two sections of lengths L_1 and L_2 with ports designated at the junctions. The sum of the two lengths must equal the circumference of the ring, i.e., $L = 2\pi r$. To obtain the unloaded ring input impedance Z_R, the input port is driven while the output port, which is arbitrarily chosen, is kept open circuited. In [5], $ABCD$ transfer matrices are derived for the individual line sections and their parallel connection is then expressed in the form of an admittance matrix, similar to the derivation presented in [4]. Finally, the admittance matrix is converted to an impedance matrix to obtain the ring's unloaded input impedance [5]

$$Z_R = \frac{1}{j\omega C_R} \tag{1}$$

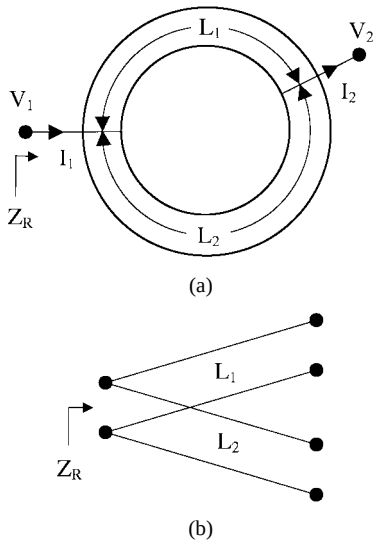

Fig. 2. Circuit models of the unloaded ring resonator, (a) Ring decomposed into two sections. (b) Transmission-line model.

where

$$C_R = \frac{2Y_0[1-\cos(2\pi\beta r)]}{\omega\sin(2\pi\beta r)} \tag{2}$$

and where Y_0 is the characteristic admittance, ω is the radian frequency, and β is the lossless propagation constant. The rather lengthy derivation is a good academic example of how transfer matrices may be used to express an input impedance; however, a far simpler technique is to consider the ring as a parallel connection of two open-circuited transmission lines, as shown in Fig. 2(b). Given the anticipated co-linear feed, the length of each line section is $L_1 = L_2 = L/2$. Transmission-line theory then allows the input impedance of the unloaded ring to be *immediately* expressed, without using (2), as

$$Z_R = \frac{Z_0}{2j}\cot\frac{\beta L}{2} \tag{3}$$

where Z_0 is the characteristic impedance. One may verify that (1) and (3) yield identical values. The unloaded ring model has recently been expanded to include loss, but the derivation again uses complicated transfer matrices [6]. The derivation may be avoided altogether because loss may be easily included in (3) by using the hyperbolic cotangent

$$Z_R = \frac{Z_0}{2}\coth\frac{\gamma L}{2} \tag{4}$$

where the familiar propagation constant is defined by $\gamma = \alpha + j\beta$. To our knowledge, (3) and (4) are by far the simplest equations presented to date. Using these expressions, one finds that the unloaded ring resonator presents an input impedance that cycles between a series and a parallel resonance as a function of frequency, presenting the former when the circumference is an odd multiple of $\lambda_g/2$ and the latter when the multiple is even, where λ_g is the guided wavelength. This is summarized by (5a) and (5b) as follows:

$$L_{0US} = (2N-1)\lambda_g/2 \tag{5a}$$

$$L_{0UP} = N\lambda_g \tag{5b}$$

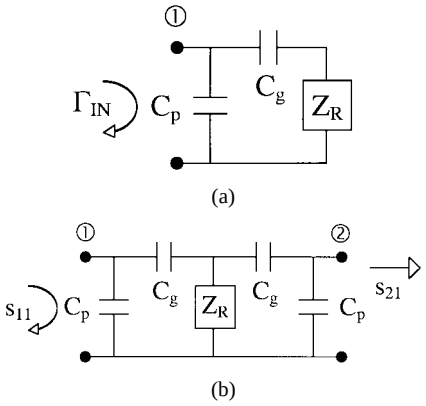

Fig. 3. Loaded ring resonator models for: (a) one-port coupling and (b) co-linear two-port coupling.

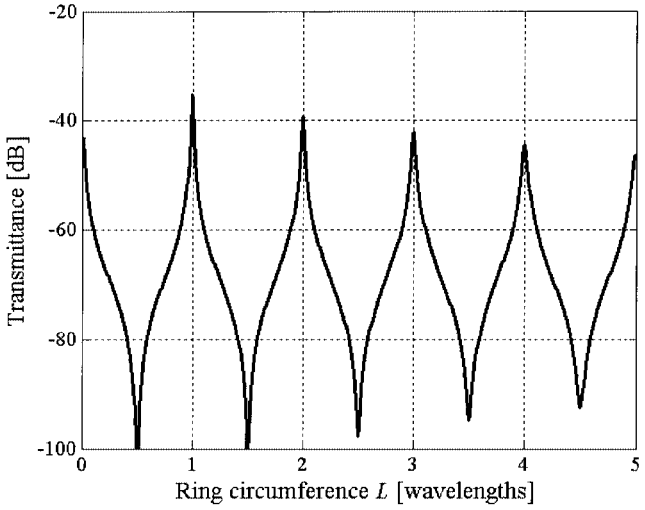

Fig. 4. Magnitude of s_{21} for the loaded two-port ring resonator of Fig. 3(b) versus the ring circumference at 5.7 GHz. The microstrip width is $W = 280$ μm, the dielectric constant is 6.15, and the substrate height is $h = 187$ μm. The coupling gap length is $S = 50$ μm and the attenuation of the microstrip is set to 0.1 dB/cm.

where N is the order of the resonance. A resonator must couple to an external circuit if it is to be sensed. In doing so, parasitic elements are introduced that perturb the unloaded behavior of the ring. It has been shown that the parasitic elements caused by the gap between the microstrip feed line and the ring may be modeled as an L-network of two capacitors, as shown in Fig. 3(a) for the one-port loaded ring [5]. As illustrated in Fig. 1, this study uses the ring as a two-port loaded resonator, therefore, the model has been extended to that shown in Fig. 3(b). Conceptually, the two-port model is justified since increasing the gap to infinity on any one side must yield the same one-port model of Fig. 3(a). A simple field analysis of the two-port ring reveals that an unloaded series resonance always produces a voltage null at the output port, meaning that a transmission null will always occur for series resonant modes. A lightly loaded two-port resonator already has near-negligible transmission levels so these nulls will be buried in the noise of the analyzer. This is illustrated in Fig. 4, where the transmittance of the two-port resonator illustrated in Fig. 3(b) is plotted versus the circumference of the ring. Only the parallel resonance modes of (5b) have voltage

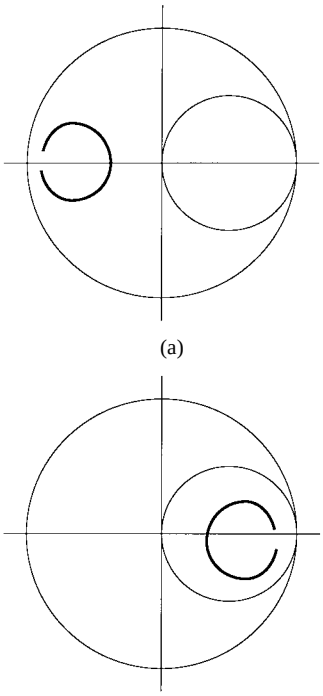

Fig. 5. Input impedance loci of undercoupled resonators. (a) Parallel. (b) Series.

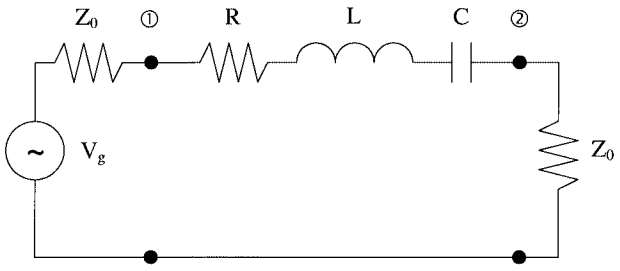

Fig. 6. Series model of the two-port ring resonator without parasitics, as seen by the external circuitry.

maxima at the output port, resulting in the characteristic transmission peaks at those resonant frequencies. Thus, the ring's fundamental resonance *must* be chosen to coincide with the parallel resonant mode or $L = \lambda_g$.

Given that the unloaded ring of Fig. 2(a) is operating in a parallel mode, one would expect the input impedance to resemble that of a lightly loaded (undercoupled) parallel resonator, similar to the one shown on the Smith chart in Fig. 5(a). In practice, this response will *not* be observed because the capacitive L-network of the input port inverts the input impedance, resulting in the reflection response shown in Fig. 5(b), which is consistent with the *series-resonant* circuit of Fig. 6. Note, however, that the L-networks are not ideal inverters and will introduce parasitic reactance to the resonator, causing the locus to skew slightly toward the capacitive side of the Smith chart. This ultimately shifts the resonant frequency, a topic that will be addressed in Section VI. Therefore, even though the unloaded ring itself is theoretically operating at what should be a parallel resonance, it appears to the external world as a series-connected series resonator. This is not surprising since, as the coupling is loosened, the input impedance must tend toward that of an open circuit, meaning that the resonance should appear on the right-hand side of the Smith chart.

III. Characterization Method

While the first objective of this study remains the modeling of the ring resonator, the second objective is the characterization of the microstrip line. In this section, the experimental method used for the latter purpose is presented, where both the loss and permittivity are obtained from the same microwave swept frequency measurement. The observed transmission peaks correspond *roughly* to the unloaded ring's parallel resonant frequencies, derived from (5b) and given by

$$f_{0UP} = \frac{cN}{L_{0UP}\sqrt{\varepsilon_{\text{eff}}}} \tag{6}$$

where ε_{eff} is the effective dielectric constant and c is the speed of light. Given the physical dimensions of the microstrip, any simple synthesis tool may then be used to convert the effective dielectric constant to the substrate's relative permittivity. As previously mentioned, the capacitive L-networks are nonideal impedance inverters and will cause the observed resonant frequency f_0 to be lower than the unloaded resonant frequency f_{0UP}. Hence, the observed resonant frequency must be corrected prior to it being used in (6) to extract the dielectric constant. Failure to do this will cause the relative permittivity of the substrate to be overestimated.

The equation relating the total attenuation of the transmission line to the unloaded quality factor has been rigorously derived in [6]. However, given that the unloaded ring model of Fig. 2(b) consists of a pair of half-wavelength transmission lines, the attenuation of the line may be simply stated as [7]

$$\alpha_T = \frac{\pi N}{Q_0 L}. \tag{7}$$

The unloaded quality factor Q_0 of a TEM line is directly proportional to frequency so the mode number N of the numerator ensures that (7) is applicable for all higher order modes. Experimentally, the unloaded quality factor is evaluated according to the following formula [8]:

$$Q_0 = \frac{Q_L}{1 - s_{21}^{\text{res}}} \tag{8}$$

where s_{21}^{res} is the magnitude of s_{21} in linear units at resonance and Q_L is the loaded quality factor, with the latter given by

$$Q_L = \frac{f_0}{\text{BW}_L} \tag{9}$$

where BW_L is the double-sided loaded bandwidth, expressed in hertz and measured at a level 3 dB below s_{21}^{res}.

IV. Physical Circuit and Loss Characterization

A 5.7-GHz microstrip ring resonator has been fabricated on Ferro A6-S low-temperature co-fired ceramic (LTCC). The microstrip substrate consists of one layer of tape, having a fired thickness h of 187 μm. The thickness of the microstrip conductor is approximately 8 μm and its measured dc conductivity is 0.8 mΩ/square, normalized to a thickness of 25.4 μm.

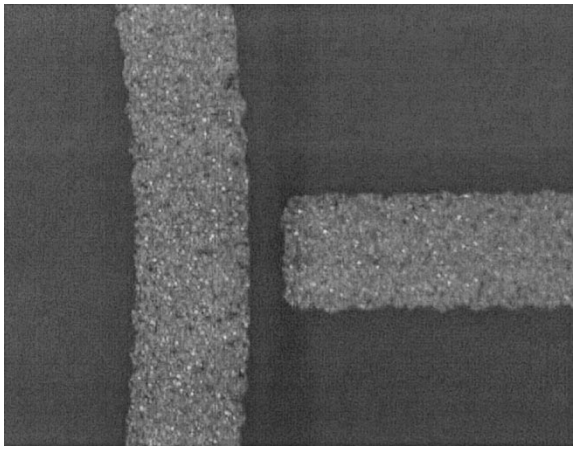

Fig. 7. Microscope photograph of one of the coupling gaps: the vertical arc is a section of the ring, whereas the horizontal line is the feed line.

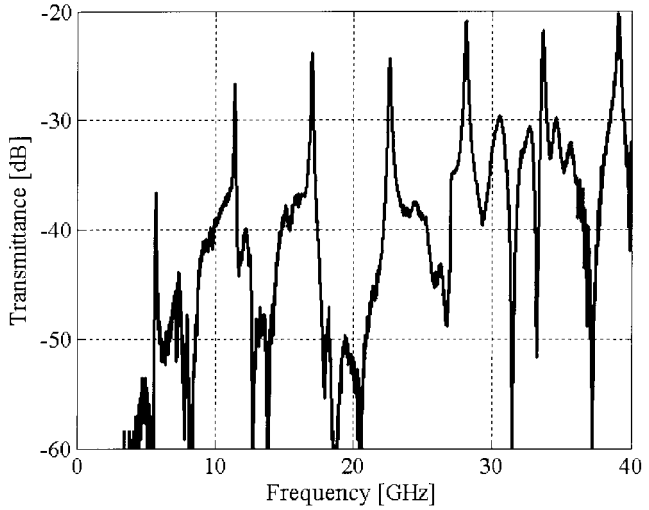

Fig. 8. Measured transmission magnitude of the 5.7-GHz ring resonator.

The width W of the microstrip line is 315 μm and the mean radius r of the ring is 3.96 mm. The gap length S between the feed lines and ring, shown in Fig. 7, is 100 μm. The measured transmission magnitude is shown in Fig. 8, where the system has been calibrated to the probe tips only. The frequency span has been broken into four separate bands with the following step sizes: 6.3 MHz between 3–8 GHz, 10 MHz between 8–16 GHz, 13.8 MHz between 16–27 GHz, and 16.2 MHz between 27–40 GHz. Such small step sizes are required to minimize the uncertainty of the attenuation constant calculation of (7). The resonant bandwidth is marginally affected by the frequency pushing effect of the capacitive loading and, thus, (7) leads directly to the total attenuation of the microstrip line, which is plotted in Fig. 9. Given the frequency step sizes listed above, the worst case error of the total attenuation constant would be $\pm$10%. However, a linear interpolation method has been used to determine the bandwidth, which reduces the error well below this estimate.

V. Lumped-Element Model Capacitance Evaluation

As previously mentioned, the observed resonant frequency must be corrected prior to its use in (6) to remove the frequency

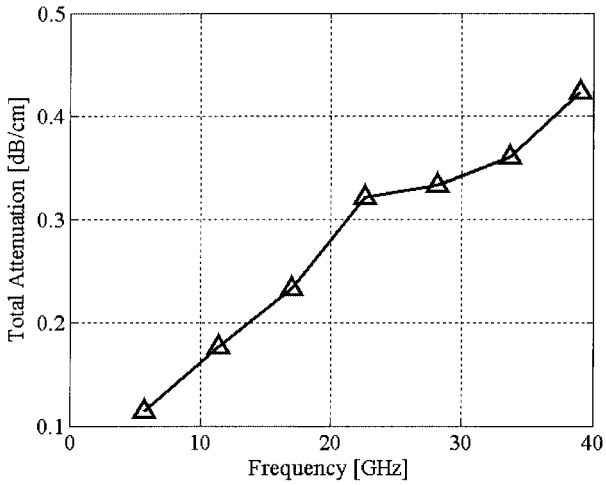

Fig. 9. Experimental attenuation of the $W = 315$ μm Ferro A6-S microstrip line versus frequency.

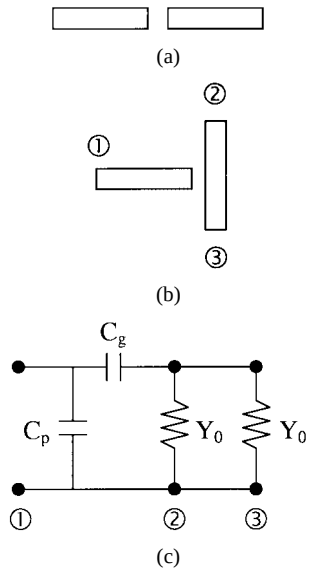

Fig. 10. Microstrip gap coupling. (a) Two-port end-to-end. (b) Three-port T-gap. (c) Equivalent lumped-element circuit for the T-gap.

pushing effects of the parasitic loading capacitors C_g and C_p of Fig. 3(b). These capacitors must be evaluated before their parasitic effects can be removed. In a previous study [5], the capacitor values were based on Gupta *et al.*'s expressions for an end-to-end microstrip discontinuity, illustrated in Fig. 10(a) [9]. Although this is a good first-order approximation, the interface of the feed line to a large-diameter ring more closely resembles a T-gap discontinuity, as shown in Fig. 10(b). This three-port T-gap may be readily simulated using a commercial 2.5-D EM solver. Based on the simulated s-parameters, the derivations found in the Appendix show that the model capacitors of Fig. 10(c) may be extracted using

$$C_g = \frac{2Y_0\,|s_{21}|}{\omega\sqrt{|1+s_{11}|^2 - |s_{21}|^2}} \tag{10a}$$

$$C_p = \frac{Y_0\,[1-s_{11}]}{j\omega\,[1+s_{11}]} - \frac{2C_gY_0}{2Y_0 + j\omega C_g} \tag{10b}$$

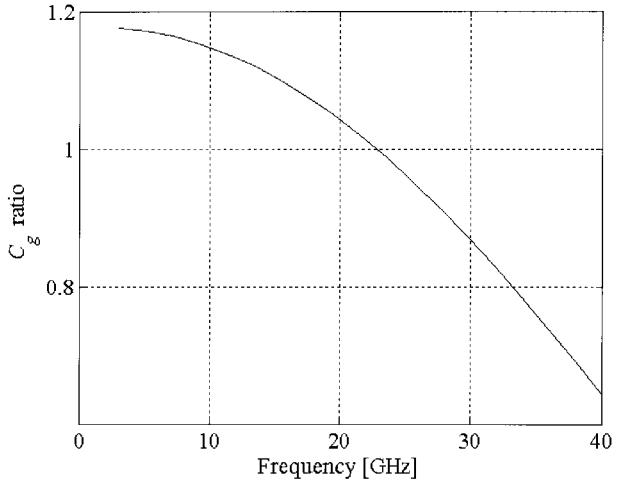

(a)

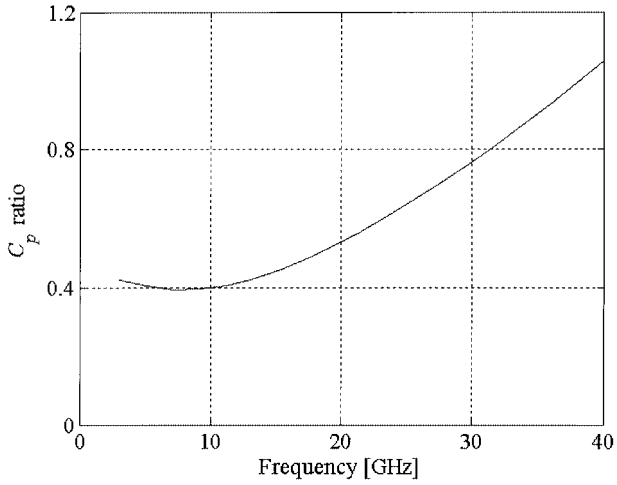

(b)

Fig. 11. Capacitor values for a 100-μm gap using the Ferro material system. (a) C_g and (b) C_p extracted from a 2.5-D simulation of the microstrip T-gap and expressed with respect to the values obtained using closed-form equations [5].

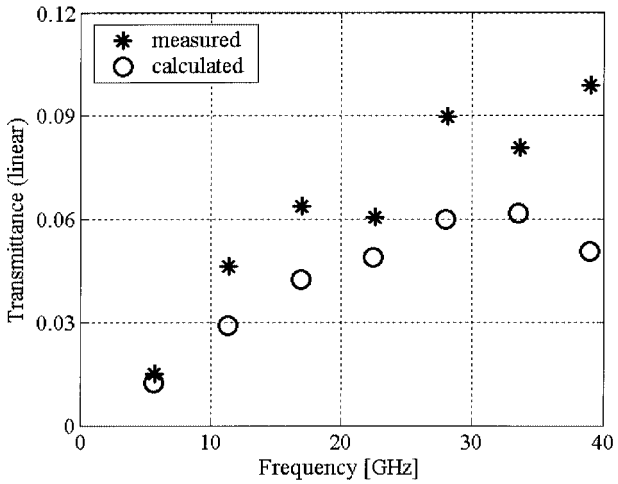

(a)

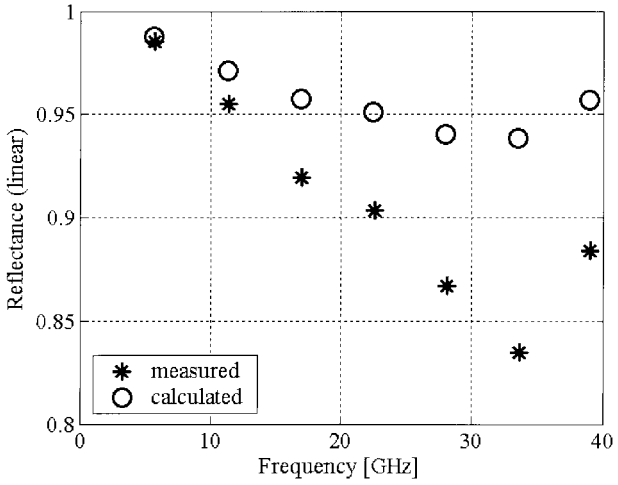

(b)

Fig. 12. Measured and calculated: (a) transmittance and (b) reflectance of the microstrip ring at resonance. The calculated values are obtained using the lumped-element ring model with capacitance values extracted from the T-gap simulations.

where s_{11} and s_{21} are the s-parameters from the 2.5-D simulator and Y_0 is the characteristic admittance. Note that the complex value of s_{11} is used in (10), meaning that s_{11} must be deembedded to the edge of the gap prior to its use. Equation (10) is general and is applicable to any microstrip T-gap.

The expressions for the end-to-end microstrip gap model as derived by Gupta *et al.* were curve fitted to data that were, in turn, calculated using quasi-static methods [9]. The resulting model does not include radiative effects. In keeping with this, the 2.5-D simulation of the T-gap has been done by enclosing the structure in a perfect electric conducting (PEC) cavity. For the Ferro system in question, the sides of the cavity are 1.7-mm long and the lid is $5h = 0.935$ mm above the substrate. A High Frequency Structure Simulator (HFSS) eigenmode simulation estimates the first cavity mode to be well beyond the maximum frequency of interest. Fig. 11 plots the extracted capacitor values with respect to those calculated using the equations found in [5], the latter being constant versus frequency with $C_g = 7.53$ fF and $C_p = 4.81$ fF. The extracted capacitor values are close to those suggested in [5], notwithstanding the frequency dependence.

A good model of the ring and coupling gaps should not only predict the resonant frequency, but should also predict the magnitude of the transmission and reflection coefficients. To date, simulated s-parameter magnitudes have not been corroborated with actual measurements [5]. Fig. 12 plots both the simulated and observed resonant transmission peaks and reflection troughs, where the simulated data have been obtained using the lumped-element model of Fig. 3(b). Good agreement is obtained between the model and measured data up to the fourth-order resonance, where reflectance errors of less than 0.5 dB and transmittance errors of less than 3.5 dB are observed. Divergence above the fourth-order resonance may be due to the presence of radiation in the physical circuits.

VI. Resonant Frequency

The frequency pushing of the coupling capacitors will now be assessed by using the lumped-element model with the extracted capacitor values. Computed polar input reflection loci of the unloaded and two-port loaded rings are shown in Fig. 13, where the dashed outer locus is that of the unloaded ring, whereas the

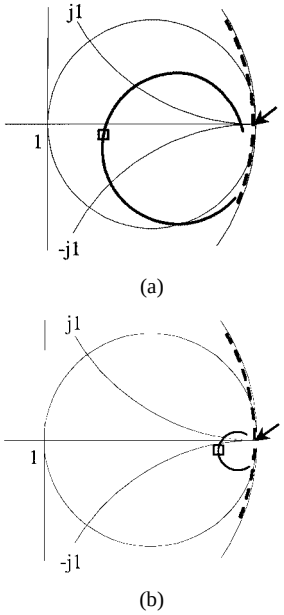

Fig. 13. Input reflection loci of ring resonators on the Smith chart. The dashed line represents the unloaded ring and is the same in both graphs, the arrow marking the unloaded parallel resonance. The solid line represents the two-port loaded ring for the cases of: (a) tight coupling and (b) loose coupling.

solid inner locus is that of the two-port loaded ring. The loaded ring is more tightly coupled in Fig. 13(a) than it is in Fig. 13(b), meaning that the gap size S would be larger for the loaded ring of Fig. 13(b). A series resonance f_s and a parallel resonance f_p can be defined for the loaded ring at points where the input reactance goes to zero [4], [5]. This happens at two frequencies on the loaded ring's locus in Fig. 13(a). If the impedance inverters were ideal, then the arrow in Fig. 13(a), which represents the parallel resonance of the unloaded ring, would occur at the same frequency as the *observed* resonance (square symbol) of the loaded ring, the latter being the minimum point of the reflection magnitude. Note, however, that the minimum reflection magnitude occurs at a frequency that is below the unloaded parallel resonant frequency. The minimum reflection coefficient occurs at a location on the locus that is slightly capacitive, in fact, the entire loaded locus is skewed slightly to the capacitive side—this is the effect of the loading capacitors, which act as nonideal impedance inverters. This means that the observed resonant frequency, represented by the square in Fig. 13(a), does not correspond exactly to what we have *defined* as being the resonance, i.e., when the input reactance X_{in} is zero.

As the coupling is reduced, the diameter of the loaded reflection locus decreases and shifts more toward the edge of the Smith chart, as shown in Fig. 13(b), which is a locus that is representative of the physical circuit under test. Not surprisingly, this causes the resonant frequencies f_s and f_p to approach each other since the length of the locus above the $X_{\text{in}} = 0$ line shrinks as the coupling is reduced. This has also been noted in [4], although the mechanism leading to this observation has not been explained. It must be said that this phenomenon is due solely to the coupling capacitors and is not an inherent property of the ring itself.

If the coupling is further reduced, there will come a point where the two previously defined resonant frequencies coincide in frequency, i.e., the locus will only touch the $X_{\text{in}} = 0$ line at one frequency. Reducing the coupling further still, the locus will no longer cross the $X_{\text{in}} = 0$ line. Conceptually this is reassuring since increasing the coupling gap means that the input feed line begins to resemble an open-ended microstrip, which is inherently capacitive. This leads to a dilemma since our previously held definitions of resonance no longer identify *any* resonant points, and yet, the transmission magnitude on the vector network analyzer (VNA) will still show a transmission peak (albeit a small one) that is consistent with resonance since there will still be a location on the locus that is closer to the center of the Smith chart than the rest.

TABLE I
FREQUENCY CORRECTION AND PERMITTIVITY OF THE 5.7-GHz RING RESONATOR

order N	1	2	3	4	5	6	7
f_0 observed [GHz]	5.70	11.40	17.00	22.60	28.11	33.64	39.07
f_{0UP} [GHz]	5.73	11.45	17.07	22.69	28.21	33.74	39.17
ε_{eff} (Equation 6)	4.428	4.435	4.490	4.518	4.567	4.597	4.643
ε_r	6.17	6.14	6.18	6.17	6.19	6.18	6.19

For the two-port loaded resonator, we must abandon the notion of being able to identify distinct series and parallel resonance points defined by $X_{\text{in}} = 0$. Instead, the resonant frequencies should be redefined as corresponding to peaks/troughs in the transmission/reflection magnitudes since these are *always* visible on the VNA. However, this latter approach is problematic because (6), which leads to the evaluation of the dielectric constant, applies only when the *unloaded* ring is at its parallel resonance point, whereas the observed resonance on the VNA does not occur at this same frequency. It is this difference that will now be assessed and is termed the *frequency correction* rule. A rule will be sought that will allow the observed resonant frequency f_0 to be converted to the unloaded ring's resonant frequency f_{0UP}. The rule is obtained by using the lumped-element model of Fig. 3(b). Simulated comparisons show that the unloaded parallel resonant frequency is up to 0.46% higher than the observed loaded resonant frequency (defined by peaks/troughs in the transmittance/reflectance) throughout the first seven harmonics that are used in this study. This percentage depends on the materials and the gap size used for a given ring resonator. Table I lists the resonant frequencies and permittivity values thus obtained for the 5.7-GHz resonator, and Fig. 14 plots the relative permittivity versus frequency. The average relative permittivity is 6.17, which is 4.6% higher than the nominal value listed for this material system [10]. Failure to correct for the capacitive loading of the circuit would have increased the average relative permittivity to approximately 6.25, a value that has been confirmed by an external laboratory [11].

VII. LUMPED-ELEMENT MODEL RESONANT-FREQUENCY PREDICTION

We close by testing the lumped-element model using the material parameters obtained from the measurements. The resulting resonant-frequency error is shown in Fig. 15, where resonance is defined by the peak/trough of the transmittance/reflectance and not by $X_{\text{in}} = 0$. The agreement between the

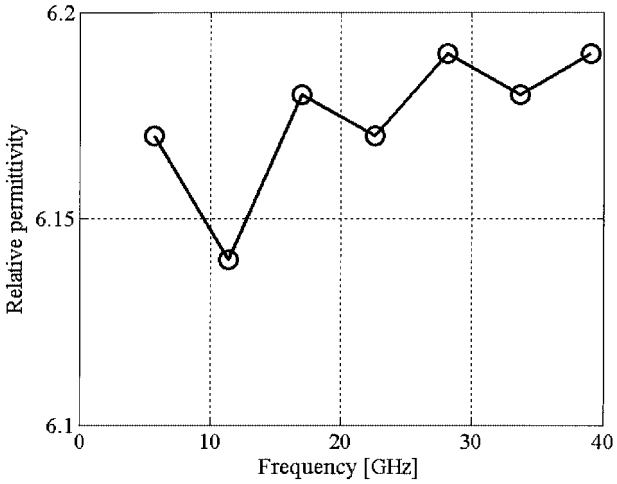

Fig. 14. Relative permittivity obtained from the ring resonator using frequency correction.

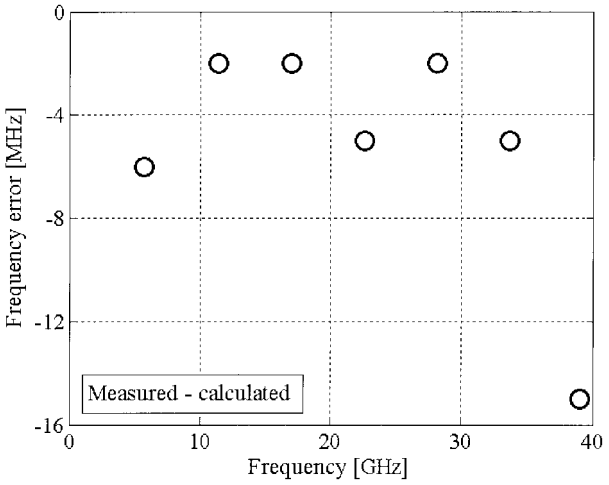

Fig. 15. Difference between the observed and calculated resonant frequencies, the latter simulated using the experimentally obtained material parameters.

calculated and observed resonant frequencies is excellent. The highest absolute error of 15 MHz occurs at 39.1 GHz and the highest relative error of 0.11% occurs at 5.7 GHz. For a simple lumped-element model to corroborate observations throughout the Ka-band is quite remarkable. Using the new relative permittivity values marginally affects the calculated reflectance and transmittance, which remain as those shown in Fig. 12.

VIII. Conclusion

In this paper, the microwave properties of a microstrip line have been obtained from a single measurement between 5–40 GHz. The simplicity of the method and of the ring resonator itself lend themselves well for general use. The relative permittivity of the substrate ranges between 6.14–6.19 and the total attenuation increases from 0.11 to 0.42 dB/cm. These values are consistent with the material specifications and have been corroborated by an external source.

Theoretically, the extended lumped-element model for the two-port co-linear-fed ring resonator has been successfully applied. The most simple derivation to date of the unloaded ring's

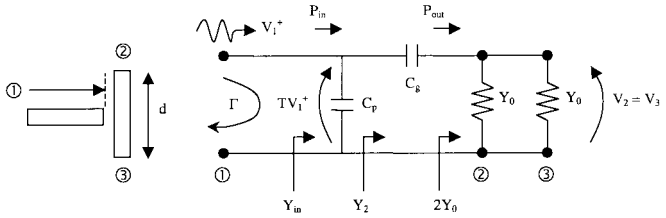

Fig. 16. Microstrip T-gap junction and its equivalent lumped-element model.

input impedance has been presented. A method for extracting the capacitance values of the loaded ring resonator from simple 2.5-D simulations has also been presented. The method not only leads to excellent resonant-frequency predictions, but also leads to good reflectance and transmittance values. For the first time, the frequency pushing effects of the lumped-element coupling circuits have been assessed and used to correct the observed resonant frequency. Finally, the mechanism responsible for the input impedance behavior of the loaded ring has also been discussed.

Appendix

Equation (10) is derived by considering the lumped-element model of the T-gap junction, which is repeated and annotated as Fig. 16. Port 1 is excited and is deembedded to the edge of the gap, whereas ports 2 and 3 are terminated in matched loads. As will be shown, the final equations are a function of the *magnitude* of s_{21} only, hence, the length d of the transmission line between ports 2 and 3 does not need to be included in the lumped-element model. The goal is to extract values of C_p and C_g based on simulated values of s_{11} and s_{21}, hence, the relationship between these four parameters must be found. We begin by evaluating the admittances, which lead directly to the reflection Γ and transmission T coefficients on port 1 as follows:

$$Y_2 = \frac{j2\omega C_g Y_0}{2Y_0 + j\omega C_g} \tag{11a}$$

$$Y_{\text{in}} = Y_2 + j\omega C_p \tag{11b}$$

$$\Gamma = \frac{Y_0 - Y_{\text{in}}}{Y_0 + Y_{\text{in}}} \tag{11c}$$

$$T = 1 + \Gamma \tag{11d}$$

where Y_0 is the known characteristic admittance of all three ports. The time-averaged real power that is delivered to the input of the circuit is given by

$$P_{\text{in}} = \frac{1}{2}\left|TV_1^+\right|^2 \Re e\left\{Y_{\text{in}}\right\} = \frac{1}{2}\left|TV_1^+\right|^2 \Re e\left\{Y_2\right\} \tag{12}$$

whereas the time-averaged real *output* power, the sum of the real power delivered to ports 2 and 3, is

$$P_{\text{out}} = \frac{1}{2}\left|V_2\right|^2 \Re e\left\{2Y_0\right\} = \left|V_2\right|^2 Y_0. \tag{13}$$

A network of purely reactive elements consumes no real power. In our case, the capacitors C_p and C_g are the only elements that exist between the reference planes for the input and output

power, hence, in terms of real power, $P_{\text{in}} = P_{\text{out}}$. This leads to the following equality, yielding the magnitude of s_{21} explicitly:

$$\left|TV_1^+\right|^2 \Re e\{Y_2\} = 2\left|V_2\right|^2 Y_0$$

$$\frac{\left|V_2\right|^2}{\left|V_1^+\right|^2} = \frac{\left|T\right|^2 \Re e\{Y_2\}}{2Y_0}$$

$$\left|s_{21}\right| = \sqrt{\frac{\left|T\right|^2 \Re e\{Y_2\}}{2Y_0}}. \tag{14}$$

To find C_g, the real part of Y_2 in (14) is isolated and (11d) is used to expand T yielding

$$\Re e\{Y_2\} = \frac{2Y_0\left|s_{21}\right|^2}{\left|1+s_{11}\right|^2}. \tag{15}$$

Next, Y_2 is expanded from (11a) so that its real part may be expressed explicitly as follows:

$$Y_2 = \frac{j2\omega C_g Y_0}{2Y_0 + j\omega C_g} = \frac{j2\omega C_g Y_0\left[2Y_0 - j\omega C_g\right]}{4Y_0^2 + \omega^2 C_g^2}$$

$$\Re e\{Y_2\} = \frac{2\omega^2 C_g^2 Y_0}{4Y_0^2 + \omega^2 C_g^2} \tag{16}$$

whereupon substitution of (16) into (15) yields

$$\omega^2 C_g^2 = \left[4Y_0^2 + \omega^2 C_g^2\right]\frac{\left|s_{21}\right|^2}{\left|1+s_{11}\right|^2}$$

$$\omega^2 C_g^2\left[1 - \frac{\left|s_{21}\right|^2}{\left|1+s_{11}\right|^2}\right] = \frac{4Y_0^2\left|s_{21}\right|^2}{\left|1+s_{11}\right|^2}$$

$$C_g^2 = \frac{4Y_0^2\left|s_{21}\right|^2}{\omega^2\left[\left|1+s_{11}\right|^2 - \left|s_{21}\right|^2\right]}$$

$$C_g = \frac{2Y_0\left|s_{21}\right|}{\omega\sqrt{\left|1+s_{11}\right|^2 - \left|s_{21}\right|^2}} \tag{10a}$$

which is the desired result for C_g. Note that only the magnitude of s_{21} is needed, whereas a complex value of s_{11} is required. The simulated value of s_{11} must, therefore, be deembedded up to the edge of the gap before it can be used in (10a).

To obtain C_p, the input admittance to the circuit is isolated from (11)

$$Y_{\text{in}} = \frac{Y_0[1-\Gamma]}{1+\Gamma}$$

$$Y_2 + j\omega C_p = \frac{Y_0[1-\Gamma]}{1+\Gamma}$$

$$C_p = \frac{Y_0[1-s_{11}]}{j\omega[1+s_{11}]} - \frac{2C_g Y_0}{2Y_0 + j\omega C_g} \tag{10b}$$

which is calculated once C_g has been found. As a verification, C_p must be purely real even though the right-hand side of (10b) is a subtraction of complex terms.

ACKNOWLEDGMENT

The LTCC modules were fabricated by Valtion Teknillinen Tutkimuskeskus (VTT) Electronics, Oulu, Finland. The authors wish to thank the staff of VTT's Manufacturing Technology Group. In particular, the authors would like to thank K. Kautio for his expertise in LTCC fabrication technology.

REFERENCES

[1] H. M. Barlow and A. L. Cullen, *Micro-Wave Measurements*. London, U.K.: Constable and Company, 1950.
[2] T. C. Edwards, *Foundations for Microstrip Circuit Design*, 2nd ed. Chichester, U.K.: Wiley, 1992, pp. 243–258.
[3] J. Carroll, M. Li, and K. Chang, "New technique to measure transmission line attenuation," *IEEE Trans. Microwave Theory Tech.*, vol. 43, pp. 219–222, Jan. 1995.
[4] K. Chang, *Microwave Ring Circuits and Antennas*. New York: Wiley, 1996, pp. 5–41.
[5] C.-C. Yu and K. Chang, "Transmission-line analysis of a capacitively coupled microstrip-ring resonator," *IEEE Trans. Microwave Theory Tech.*, vol. 45, pp. 2018–2024, Nov. 1997.
[6] L.-H. Hsieh and K. Chang, "Equivalent lumped elements G, L, C, and unloaded Q's of closed- and open-loop ring resonators," *IEEE Trans. Microwave Theory Tech.*, vol. 50, pp. 453–460, Feb. 2002.
[7] D. M. Pozar, *Microwave Engineering*, 1st ed. Reading, MA: Addison-Wesley, 1990, pp. 341–342.
[8] D. A. Rudy, J. P. Mendelsohn, and P. J. Muniz, "Measurement of the RF properties with series resonant microstrip elements," *Microwave J.*, vol. 41, pp. 22–41, Mar. 1998.
[9] K. C. Gupta, R. Garg, and I. J. Bahl, *Microstrip Lines and Slotlines*. Dedham, MA: Artech House, 1979, pp. 107–136.
[10] "A6-S tape, LTCC tape system," Mater. Group, Ferro Corporation, Vista, CA, Mater. Specification Sheet, rev. 1000, 2000.
[11] R. Kulke *et al.*, "Investigation of ring-resonators on multilayer LTCC," presented at the IEEE MTT-S Int. Microwave Symp. Workshop, Phoenix, AZ, 2001.

Joey R. Bray (S'96) received the B.A.Sc. and M.A.Sc. degrees in electrical engineering from the University of Ottawa, Ottawa, ON, Canada, in 1995 and 1998, respectively, and is currently working toward the Ph.D. degree in microwave engineering at Carleton University, Ottawa, ON, Canada.

From 2001 to 2002, he was a Visiting Researcher with Valtion Teknillinen Tutkimuskeskus (VTT) Electronics, Oulu, Finland, where he was involved with the microwave characterization of LTCC circuits and materials. His research interests include ferrite microwave devices, microwave passive devices, and antenna design.

Mr. Bray was the recipient of a 2001 Graduate Fellowship Award presented by the IEEE Microwave Theory and Techniques Society (IEEE MTT-S).

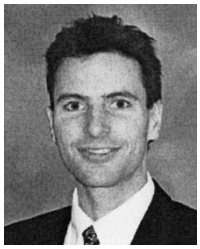

Langis Roy (M'94) received the B.A.Sc. degree in electrical engineering from the University of Waterloo, Waterloo, ON, Canada, in 1987, and the M.Eng. and Ph.D. degrees from Carleton University, Ottawa, ON, Canada, in 1989 and 1993, respectively.

Following a research fellowship with Matra Marconi Space France in 1993, he joined the Department of Electrical Engineering, University of Ottawa, as an Assistant Professor. Since 1999, he has been an Associate Professor with the Department of Electronics, Carleton University. His research interests are GaAs monolithic integrated circuits, high-performance microwave circuit packaging, integrated active antennas, and numerical techniques in electromagnetics.

Dr. Roy is a Licensed Professional Engineer in the Province of Ontario.